

Revisiting model self-interpretability in a decision-theoretic way for binary medical image classification

Sourya Sengupta¹ and Mark A. Anastasio^{1,2}

¹Department of Elec. & Computer Eng., University of Illinois Urbana-Champaign, IL, USA

¹Department of Bioengineering, University of Illinois Urbana-Champaign, IL USA

²Department of Computer Science, University of Illinois Urbana-Champaign, IL USA

March 14, 2023

Abstract

Interpretability is highly desired for deep neural network-based classifiers, especially when addressing high-stake decisions in medical imaging. Commonly used post-hoc interpretability methods may not be always useful because different such methods can produce several plausible but different interpretations of a given model, leading to confusion about which one to choose. In this work, an inherently interpretable encoder-decoder model coupled with a single-layer fully connected network with unity weights is proposed for binary medical image classification problems. The feature extraction component of a trained black-box network for the same task is employed as the pre-trained encoder of the interpretable model. The model is trained to estimate the decision statistic of the given trained black-box deep binary classifier to maintain a similar accuracy. The decoder output represents a transformed version of the to-be-classified image that, when processed by the fixed fully connected layer, produces the same decision statistic value as the original classifier. This is accomplished by minimizing the mean squared error between the decision statistic values of the black-box model and encoder-decoder based model during training. The decoder output image is referred to as an *equivalency map*. Because the single-layer network is fully interpretable, the equivalency map provides a visualization of the transformed image features that contribute to the decision statistic value and, moreover, permits quantification of their relative contributions. Unlike the traditional post-hoc interpretability methods, the proposed method is inherently interpretable, quantitative, and fundamentally based on decision theory.

Keywords: Decision theory, interpretability, deep learning, medical imaging

1 Introduction

Despite showing excellent potential for performing important tasks such as image classification and object detection, deep learning models are often criticized as being black-boxes that cannot be interpreted. As such, the development of post-hoc interpretability methods for explaining black-box models for mission-critical applications that include medical imaging remains an active research topic [1, 2, 3]. However, such methods may not provide a reliable interpretation of how the black-box models arrived at their decisions. This is because many convincing but different explanations or interpretations can be produced [4] and it is not always clear which interpretation is "correct" among them. This can clearly confound the goal of interpreting a black box model. There exist self-interpretable deep learning models, but many of them suffer from an interpretability-performance

trade-off. These self-interpretable models can be less expressive and can result in a drop in performance compared to their black-box counterparts[5, 6, 7]. Hence, there is an urgent need for the development of alternative methods for achieving inherent self-interpretability and maintain the performance of a corresponding traditional classifier.

Unlike traditional post-hoc methods, our approach is fundamentally based on the intersection of decision theory and deep learning. In this work, the following problem is addressed: *Assume a deep binary black-box medical image classifier is provided. Find an alternative inherently interpretable or self-interpretable network that yields a similar classification performance as the black-box model.* To accomplish this, the original network is re-expressed in the form of an encoder-decoder model coupled with a single-layer fully connected network with unity weights. This model is trained in such a way that the output of the decoder, referred to as an *equivalency map* below, represents a transformed version of the to-be-classified image whose element-wise sum produces the same decision statistic value as the original classifier. As such, the equivalency map provides a quantitative and a novel means of understanding how the transformed image features contribute to the decision statistic value.

2 Methodology

From the perspective of decision theory, a binary classification of an image $f \in \mathbb{R}^N$ involves computation of a scalar-valued decision statistic $t = h(f)$, where $h(f)$ is referred to as the discriminant function. For a linear classifier, the decision statistic for an image can be formulated as $t = h(f) = w^\dagger f + b$, where $w \in \mathbb{R}^N$ is called the decision template. Without loss of generality, we assume $b = 0$. This mapping can also be expressed as

$$t = w^\dagger f = e^\dagger [w \odot f], \quad (1)$$

where $e \in \mathbb{R}^N$ is a vector of all 1s and \odot denotes the Hadamard product. This model is self-interpretable because $w \odot f$ can be readily visualized to understand the features used by the classifier for the decision.

For a non-linear classifier $h_{nl}(\cdot)$, the decision statistic t for a given image f can be expressed as $t = h_{nl}(f)$, where the subscript nl denotes that the discriminant function is non-linear. Inspired by Eq. (1), the decision statistic for the non-linear classifier can be re-expressed as

$$t = e^\dagger T(f), \quad (2)$$

where $T : \mathbb{R}^N \rightarrow \mathbb{R}^N$ is a non-linear mapping that maps the input image f into a transformed image $T(f)$. The decision statistic value is computed by taking element-wise summation of $T(f)$.

Consider that a deep neural network is employed to represent the discriminant function $h_{nl}(f)$. In this case, directly interpreting $h_{nl}(f)$ is known to be problematic. However, a key observation is that Eq. (2) provides an interpretable alternative form of the black-box non-linear classifier. In this alternative form, the decision statistic t can be computed by the element-wise summation of the image $T(f)$ for a given image f . For a non-linear classifier, $T(f)$ can be thought of as a generalization of the quantity $w \odot f$ in Eq. (1). According to Eq. (2), $T(f)$ represents a transformed, or equivalent, version of the to-be-classified image that, when subject to an elementwise summation by a linear single layer neural network (SLNN) with unity weights, produces the decision statistic value prescribed by the original discriminant function $h_{nl}(f)$. We therefore refer to $T(f)$ as an equivalency map (E-map). Because the subsequent SLNN is fully interpretable, the E-map provides a visualization of the transformed image features that contribute to the test statistic value and,

moreover, permits quantification of their relative contributions. Below, the means by which the E-map can be computed is described.

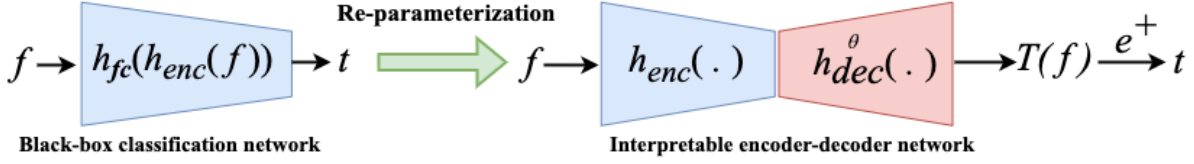


Figure 1: The black-box classification network (left) and re-parameterized interpretable model involving an encoder-decoder network (right)

3 Equivalency Map Computation

Consider that a non-linear discriminant function $h_{nl}(f)$ is represented as a composition of a feature extracting encoder network (h_{enc}) and a fully connected network (h_{fc}):

$$t = h_{nl}(f) \equiv h_{fc}(h_{enc}(f)). \quad (3)$$

This configuration is referred to as the 'original' classifier, which is assumed to be trained and provided. As depicted in Fig. 1, the key contribution of this work is to establish an alternative configuration of the original classifier, henceforth termed as the estimation network or interpretable encoder-decoder network, which can be interpreted via an E-map according to Eq. (2). To accomplish this, we approximate $T(f)$ in Eq. (2) by use of an encoder-decoder network, where the encoder is non-trainable and corresponds to h_{enc} employed by the original classifier. Hence, only the decoder network is trainable and $T(f)$ is approximated as

$$T(f) = h_{dec}^{\theta^*}(h_{enc}(f)), \quad (4)$$

where $h_{dec}^{\theta^*}(\cdot)$ represents the decoder network that is parameterized by the weights θ^* . Because, in this work, we seek to maintain the performance of the original classifier, the decoder parameters are estimated in such a way that $e^\dagger h_{dec}^{\theta^*}(h_{enc}(f)) \approx h_{nl}(f) = t$:

$$\theta^* = \arg \min_{\theta} E_{f \sim D} \left\{ L(h_{nl}(f), e^\dagger h_{dec}^{\theta}(h_{enc}(f))) \right\}. \quad (5)$$

Here, D denotes the distribution of the training images f and L denotes the loss function, which corresponds to mean squared error (MSE) in this case. It should be noted that no image labels are used during the training of the estimation network.

4 Experiments

Three different binary classification tasks were considered to evaluate and investigate the classification performance of the estimation networks in terms of accuracy. For each case, the corresponding E-maps of both normal and abnormal cases were analyzed.

4.1 Datasets

One simulated dataset and two clinical datasets were employed in the numerical studies.

Simulated mammography dataset: A tumor detection task was explored using a simulated digital mammography dataset. The double-lobed clustered lumpy backgrounds (CLB) were used as background images [8]. The to-be-detected signal was generated as a 2D symmetric Gaussian function and was inserted [9] into the background in one of the 9 discrete locations shown in Fig. 2. The images were of size 128 X 128.

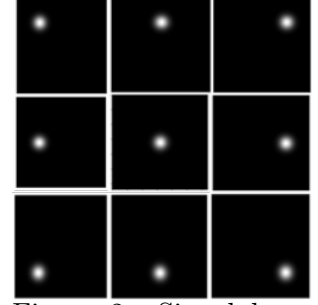


Figure 2: Signal locations

OCT dataset for Drusen detection: A Drusen detection task was performed using optical coherence tomography (OCT) images of the human retina of size 256 x 256 [10]. Drusen is characterized as accumulation of extra-cellular materials between the retinal pigment epithelium (RPE) layer and the Bruch’s membrane layer of the human retina and can be well observed using retinal OCT images.

Chest X-ray dataset for cardiomegaly detection: A cardiomegaly detection task was performed using chest x-ray images of size 1024 X 1024 images. Cardiomegaly refers to enlargement of the heart, which is a biomarker for heart diseases. The images were taken from a publicly available NIH database [11]. The image labels were created using text mining from radiological reports generated by clinicians.

Sample images from all the datasets are shown in Fig. 3, where the red bounding boxes are annotations that indicate the specific region where the abnormality is present.

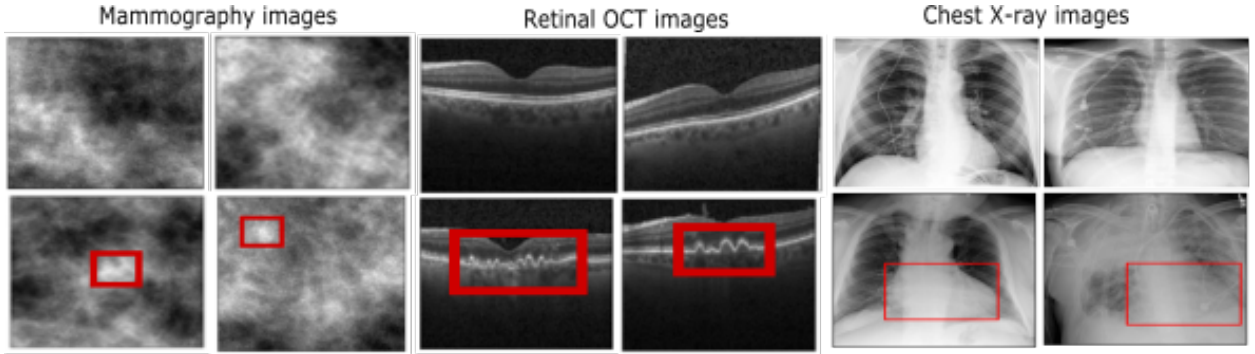


Figure 3: Example image of all datasets. Top row: normal images, bottom row: abnormal images. The red bounding boxes indicate the regions of abnormality.

4.2 Training Details

For the tumor detection and drusen detection tasks, the training, validation, and testing sets comprised 19000, 1000, and 1000 paired images, respectively. For the cardiomegaly detection task, 2000, 200 and 200 paired images were used for the training, validation, and testing respectively. For the black-box classifiers, two different configurations were used in our experiments for all three tasks. The first classifier (baseline) consisted of 3 convolutional blocks (convolution + non-linear activation) followed by a max-pool layer and two fully connected dense layers. The VGG16 network [12] was used as another black-box deep network. In each case, the feature extraction component of the black-box network was employed as the pre-trained encoder of the estimation network. The decoder of the estimation network for the baseline classifier consisted of 1 deconvolutional block (1 transposed convolutional layer + 5 convolutions + non-linear activation). In the estimation network corresponding to VGG16 black-box classifier, the number of transposed convolutional layers was the same as the number of max-pool layers in the encoder to keep the spatial dimension of the decoder output the same as the original image. For this, 5 deconvolutional blocks were used in the decoder

of the estimation network (Details in Appendix B). A final dense layer was used that performed element-wise sum of the decoder output to compute the decision statistic. Binary cross-entropy was used as the loss function for the black-box classifiers and mean squared error (MSE) was used as the loss function for the estimation network. The Adam optimizer [13] with a learning rate of $3e-5$ was used to train all the models.

4.3 Performance of the Estimation Network

Table 1: Quantitative Performance of the Estimation Networks

Dataset	Classifier	Accuracy %		Decision Statistic Estimation Error
		Classification Network	Estimation Network	
Mammography	Baseline	77.8	77.8	0.001
	VGG16	79.8	79.7	0.003
Retinal OCT	Baseline	99.1	99.1	0.0005
	VGG16	99.5	99.5	0.0004
Chest X-ray	Baseline	78.4	78.3	0.003
	VGG16	81.2	81.0	0.003

For all the classification tasks, the accuracy and decision statistic estimation error were computed. For the estimation network, the accuracy was computed by thresholding the estimated decision statistics with a threshold value of 0.5. The estimation error was calculated by computing mean squared error (MSE) between the decision statistics generated by the original classifier and the estimation network. Table 1 contains the quantitative results for all the classifiers for the three tasks. It can be observed that the accuracy achieved by the estimation network was similar to the original classifier for all the cases.

4.4 Visualizing Equivalency Maps

Figure 4 shows examples of heatmaps generated by different state-of-the-art post-hoc interpretability methods for a tumor-present mammography image. For the trained 3 layer classifier (baseline) applied to normal vs tumor mammography classification task, methods like Saliency map, Grad-CAM, SmoothGrad, Layer-wise Relevance Propagation (LRP), Integrated Gradients [1] were used to interpret the classifier.

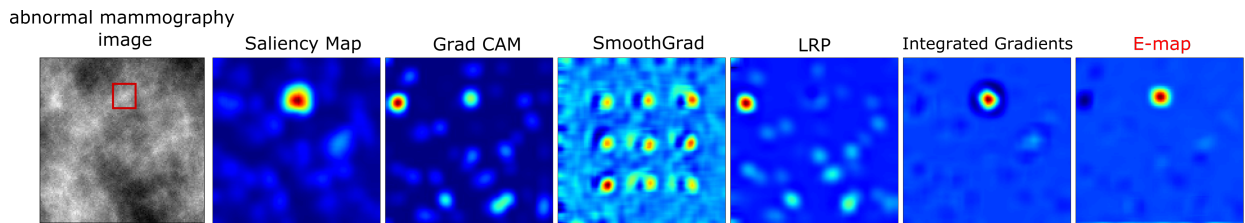


Figure 4: Different heatmap interpretations generated by different post-hoc interpretability methods. The E-map is shown on the far-right.

It was observed that different methods could yield multiple convincing but different visualizations when an abnormal mammography image was considered, which can confound model interpretation. Also shown in this figure is the E-map. The E-map is qualitatively similar to several of

the other visualizations, but can be interpreted quantitatively and is immediately yielded by the encoder-decoder based model without post-hoc processing. This can provide a more inherent and reliable means of interpretability. Figures 5 and 6 show examples of E-maps, overlayed with the original images for abnormal and normal classes, respectively, for all the datasets. The E-maps tend to find relevant regions where the abnormality is present in the abnormal images. It was also observed that, for the abnormal images, the E-map tended to have positive values (bright pixels) at the locations of abnormal features. These pixels contributed significantly to the decision statistic, yielding relatively large decision statistic values that resulted in the classification of the images as abnormal. On the other hand, the images from normal class did not show specific patterns and yielded lower decision statistics values. E-maps for VGG16 network are shown in the appendix section.

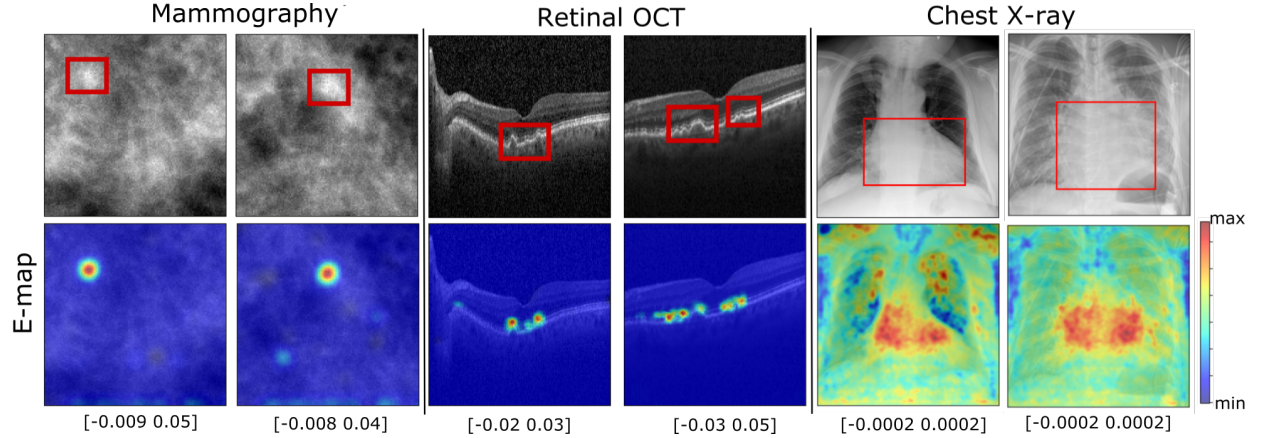


Figure 5: Top row: sample images for abnormal classes from the datasets. Bottom row: the corresponding E-maps overlayed on the original image. For the abnormal class images, E-maps tend to show regions where an abnormality is present. The red bounding boxes show the region of the abnormality. The pixel intensity value range of the E-map is shown below for each E-map. The colorbar is shown in the extreme right and applies to all E-maps.

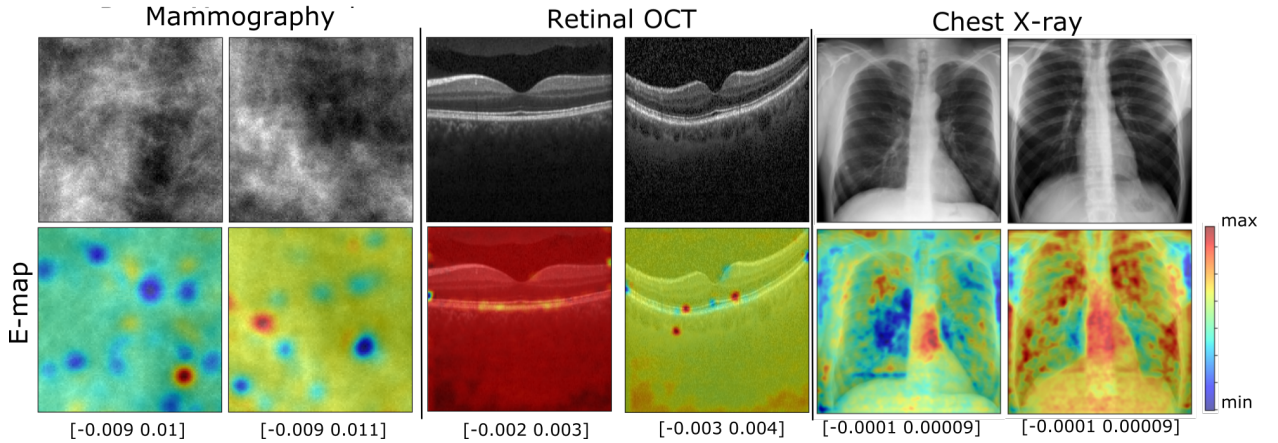


Figure 6: Top row: sample images for normal classes from the datasets. Bottom row: the corresponding E-maps overlayed on the original image. The pixel intensity value range and colorbar are shown similarly like Fig. 5.

4.5 Quantitatively Evaluating Interpretability

As elementwise summation of the E-map results in decision statistic value for a particular image, the E-map can provide quantitative insights regarding the decision of a network.

4.5.1 Pixel Intensity Distribution Analysis

As the original black-box classifiers were trained using labels 0 and 1 for normal and abnormal images, the decision statistic values for true positive cases were larger than true negative cases. This pixel intensity distribution analysis can reveal insights about how the pixel intensity distribution varies between E-maps of normal and abnormal images and how the different elements contributed towards a decision in a positive or negative manner for different cases.

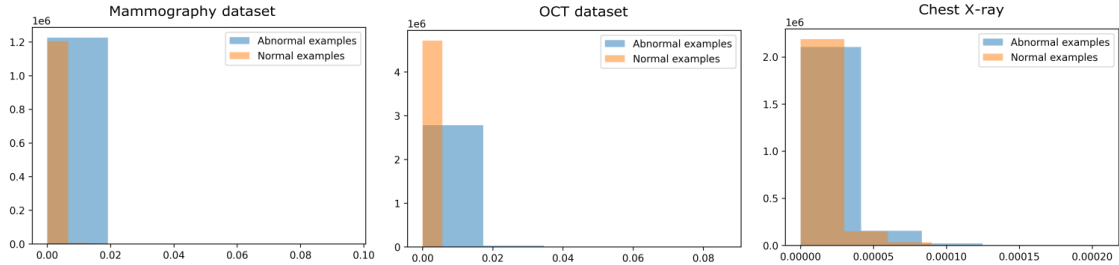


Figure 7: The pixel-intensity analysis of normal vs abnormal cases for each task

As an elementwise sum of an E-map yields the decision statistic, any positive element of an E-map contributes to classifying the image as abnormal. The negative elements act in a reverse way by minimizing the decision statistic to predict the image as a normal case. In Fig. 7, the histogram is plotted for positively contributing pixels of E-maps of normal and abnormal images of different tasks. It can be seen that there is a significant difference in positively contributing element values for abnormal cases compared to the normal images.

4.5.2 E-map Contribution from Abnormality Regions

The mammography dataset was simulated and hence the specific tumor regions were known. The NIH chest x-ray dataset had bounding box annotations for the cardiomegaly class. For these two datasets, the percentage overlap between the abnormal region and contributing pixels was computed. This quantitative study shows how many top contributing pixels of an E-map overlap with the actual abnormality region. As our method is quantitative, overlap between the disease region and contributing pixel toward decision statistics can be quantitatively determined. Figure 8 reveals how the top 1 percentile contributing pixels (red) overlap with the abnormal locations for mammography and chest x-ray dataset respectively. The percentage overlap is written above each image. Quantitative comparisons with traditional interpretability methods for the corresponding black-box classifier and chest x-ray dataset are shown in the Appendix C section.

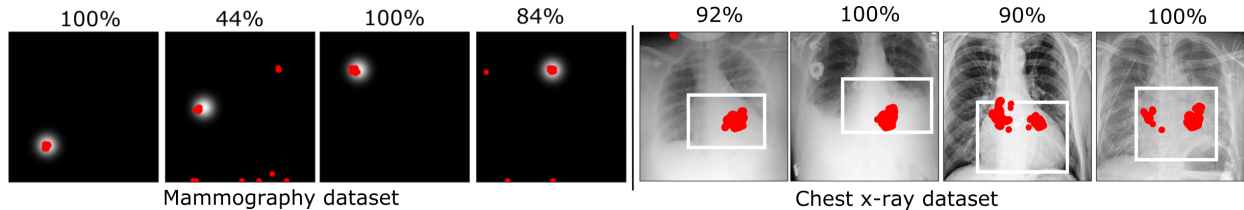


Figure 8: Examples of overlap between most contributing 1 percentile elements of E-map and the abnormal region. The red pixels are from the E-map.

4.6 Effect of Direct Training of Estimation Network

In our training framework, the estimation network employs a pre-trained encoder and it was trained using a task of estimating decision statistics. An alternative approach can be to directly train the encoder-decoder-based model by the use of the original image labels 0,1 and a classification loss. While direct training of the proposed model may also yield a similar level of interpretability, we showed a scenario where it may harm the classification performance in terms of accuracy. For the cardiomegaly detection task, Table 2 shows how direct training of the encoder-decoder based model with a classification loss and 0,1 labels can degrade the performance compared to the corresponding black-box model. This could be because the pre-training helped to provide a better weight initialization for the interpretable estimation network to learn the decision statistics. On the other hand, the proposed decision-theory inspired training scheme achieved a similar level of accuracy compared to the traditional black-box network.

Table 2: Effect of direct training of estimation network

Task	Black-box Classifier (%)	Estimation Network (%)	Direct Training
Cardiomegaly Detection	78.4	78.3	73.2

5 Conclusion

A novel decision-theory inspired method was established to provide an inherent means of self-interpretability for binary medical image classification. The proposed method involves training an interpretable encoder-decoder-based model followed by a non-trainable fully connected layer with fixed unity weights. This network employed a pre-trained encoder from a black-box classifier and the model was trained using an estimation task to estimate the decision statistic to maintain the accuracy of a given trained black-box deep binary classifier. By construction, the element-wise summation of the decoder output of the re-parameterized interpretable network represents the decision statistic value. It should be noted that there is no guarantee that the E-map $T(f)$ will always clearly reveal the spatial signatures (features) in the original image f that are important to the classifier. However, in our studies conducted to-date, we have generally found that $T(f)$ does indeed reveal the regions in f where the abnormality is present. Moreover, by construction, our method holds inherent self-interpretability in the sense that each element in the E-map contributes to the decision statistic directly.

Acknowledgements

This work is supported by NIH awards 1P41EB031772, 5R01CA238191, EB020604, EB023045, NS102213, EB028652, EB025829, R01CA233873. Research reported in this publication was supported by the National Institute Of Biomedical Imaging And Bioengineering of the National Institutes of Health under Award Number T32EB019944. The content is solely the responsibility of the authors and does not necessarily represent the official views of the National Institutes of Health.

References

- [1] A. Singh, S. Sengupta, and V. Lakshminarayanan, “Explainable deep learning models in medical image analysis,” *Journal of Imaging*, vol. 6, no. 6, p. 52, 2020.
- [2] W. Jin, X. Li, M. Fatehi, and G. Hamarneh, “Guidelines and evaluation of clinical explainable ai in medical image analysis,” *Medical Image Analysis*, vol. 84, p. 102684, 2023.
- [3] Y. Zhang, P. Tiño, A. Leonardis, and K. Tang, “A survey on neural network interpretability,” *IEEE Transactions on Emerging Topics in Computational Intelligence*, 2021.
- [4] C. Rudin, “Stop explaining black box machine learning models for high stakes decisions and use interpretable models instead,” *Nature Machine Intelligence*, vol. 1, no. 5, pp. 206–215, 2019.
- [5] Y. Wang and X. Wang, “Self-interpretable model with transformation equivariant interpretation,” *Advances in Neural Information Processing Systems*, vol. 34, pp. 2359–2372, 2021.
- [6] W. J. Murdoch, C. Singh, K. Kumbier, R. Abbasi-Asl, and B. Yu, “Interpretable machine learning: definitions, methods, and applications,” *arXiv preprint arXiv:1901.04592*, 2019.
- [7] M. Du, N. Liu, and X. Hu, “Techniques for interpretable machine learning,” *Communications of the ACM*, vol. 63, no. 1, pp. 68–77, 2019.
- [8] C. Castella, K. Kinkel, F. Descombes, M. P. Eckstein, P.-E. Sottas, F. R. Verdun, and F. O. Bochud, “Mammographic texture synthesis: second-generation clustered lumpy backgrounds using a genetic algorithm,” *Optics express*, vol. 16, no. 11, pp. 7595–7607, 2008.
- [9] M. Ruschin, A. Tingberg, M. Båth, A. Grahn, M. Håkansson, B. Hemdal, and I. Andersson, “Using simple mathematical functions to simulate pathological structures—input for digital mammography clinical trial,” *Radiation protection dosimetry*, vol. 114, no. 1-3, pp. 424–431, 2005.
- [10] D. S. Kermany, M. Goldbaum, W. Cai, C. C. Valentim, H. Liang, S. L. Baxter, A. McKeown, G. Yang, X. Wu, F. Yan, *et al.*, “Identifying medical diagnoses and treatable diseases by image-based deep learning,” *Cell*, vol. 172, no. 5, pp. 1122–1131, 2018.
- [11] X. Wang, Y. Peng, L. Lu, Z. Lu, M. Bagheri, and R. M. Summers, “Chestx-ray8: Hospital-scale chest x-ray database and benchmarks on weakly-supervised classification and localization of common thorax diseases,” in *Proceedings of the IEEE conference on computer vision and pattern recognition*, pp. 2097–2106, 2017.
- [12] A. Krizhevsky, I. Sutskever, and G. E. Hinton, “Imagenet classification with deep convolutional neural networks,” *Communications of the ACM*, vol. 60, no. 6, pp. 84–90, 2017.

- [13] D. P. Kingma and J. Ba, “Adam: A method for stochastic optimization,” *arXiv preprint arXiv:1412.6980*, 2014.

Appendix A.

Equivalency Maps for VGG Network

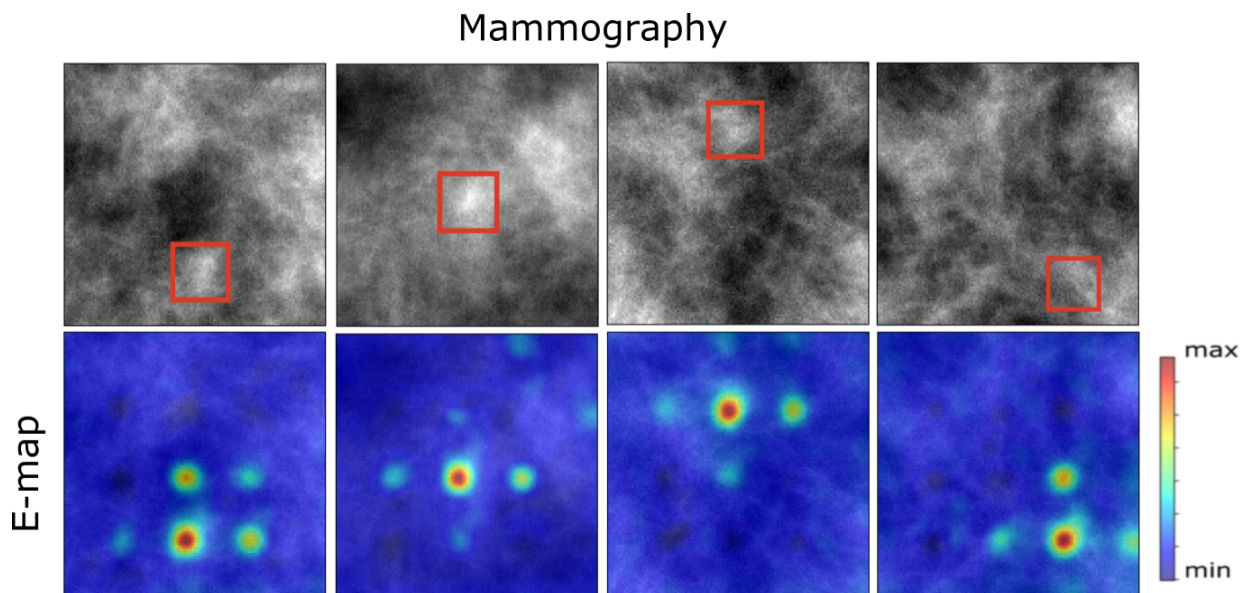


Figure 9: Top row: Sample images of abnormal classes from mammography dataset. Bottom row: The corresponding E-maps overlayed on the original image.

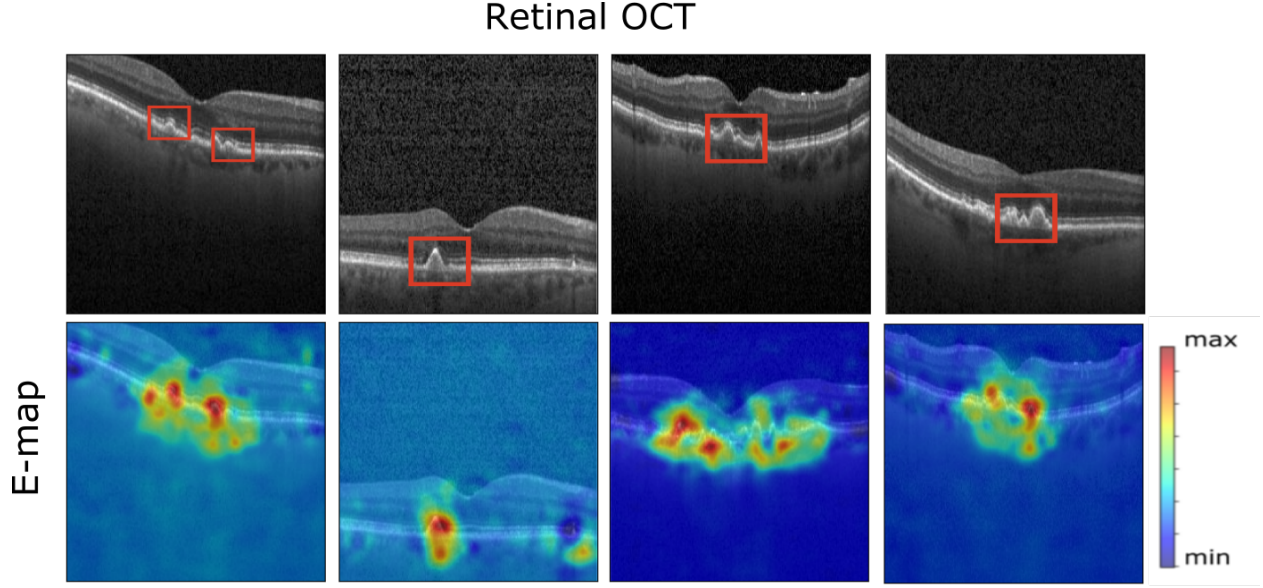


Figure 10: Top row: Sample images of abnormal classes from OCT dataset. Bottom row: The corresponding E-maps overlaid on the original image.

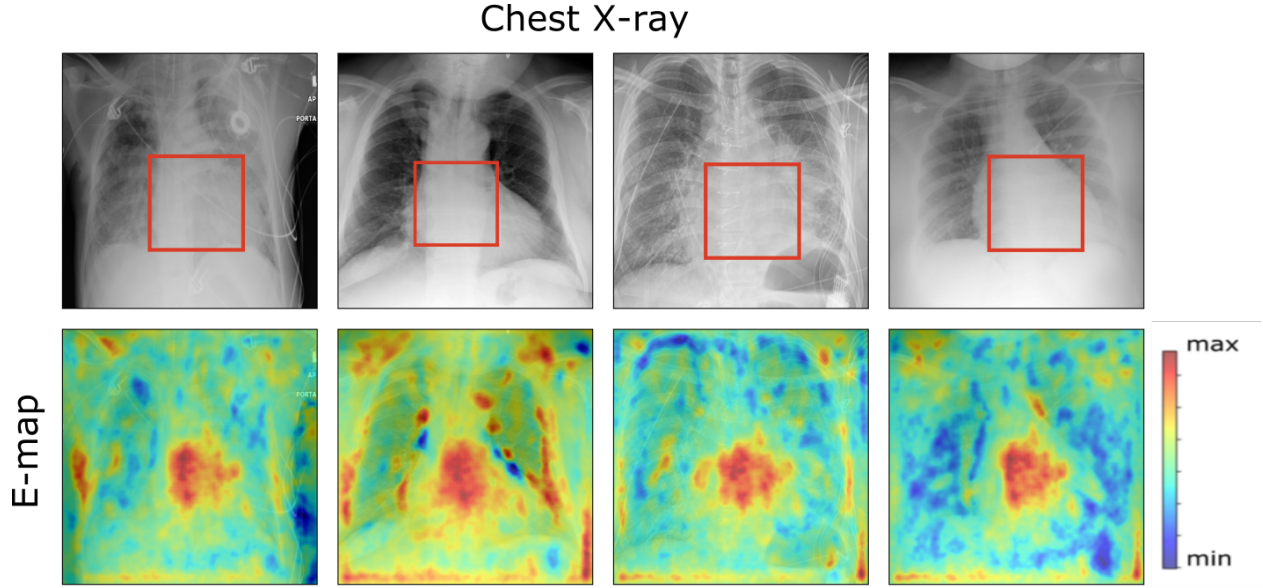


Figure 11: Top row: Sample images of abnormal classes from Chest X-ray dataset. Bottom row: The corresponding E-maps overlaid on the original image.

Appendix B.

As written in the *Training Details (Sec 4.2)*, the decoder consisted of multiple deconvolutional blocks and one penultimate convolution layer before the last layer. The details of the layers are given in the table.

Table 3: Decoder architecture details

	Type	Number of feature maps	Kernel size	Stride	Activation
Deconv block	Transposed Convolution	128	(2,2)	2	-
	Convolution X5	128, 128, 128, 64, 64	(3,3)		ReLU
Penultimate layer	Convolution	1	(3,3)		ReLU

Appendix C.

Quantitative Comparisons with Post-hoc Interpretability Methods

Our method has significant differences from post-hoc interpretability methods like CAM-based methods in terms of formulation. 1. Our method does not seek to interpret a black-box network. Rather the method is inherently interpretable as the proposed network produces an image (E-Map) whose elements are summed to form the final decision statistic and also it obtains a similar quantitative performance to the original black-box network. The post-hoc interpretability methods like Grad-CAM aim to interpret a black-box network. These post-hoc methods can provide varying interpretations for a single given black-box classifier, which can be a potential issue in deciding which method to rely upon. Still, in this section, quantitative analysis was performed to compare our method with other post-hoc interpretability methods in terms of quantitative performance. As the chest-xray dataset associated with the cardiomegaly detection task has radiologists’ annotations, this dataset was used to compare the methods in a quantitative manner. Figures 12-16 show some examples of percentage overlap between the top 1 percentile contributing pixels of the interpretability heatmaps for the black-box classifier and the abnormal region of the original image. A similar analysis was done for the E-maps. It can be observed, that in most cases percentage overlap is higher in the E-map than in most of the post-hoc interpretability methods. It should also be noted how interpretations can vary for a single black-box classifier, which can be a potential issue in deciding which method to rely upon. Table 4 shows a population level analysis of average percentage overlap between the top 1 percentile pixels of E-maps of our encoder-decoder based models and the post-hoc interpretability methods for corresponding black-box classifier with clinically annotated regions in the original abnormal images- population-level analysis over all 100 test images. The superiority of our method can be shown from the values in the table.

Table 4: Average percentage overlap with the top 1 percentile pixels of interpretation maps and clinically annotated regions in the original abnormal images- population-level analysis over all test images

	E-map	Guided Backprop	Integrated Gradients	LRP	Saliency Maps	Grad-CAM
Percentage Overlap	89%	71%	84%	83%	30%	12%

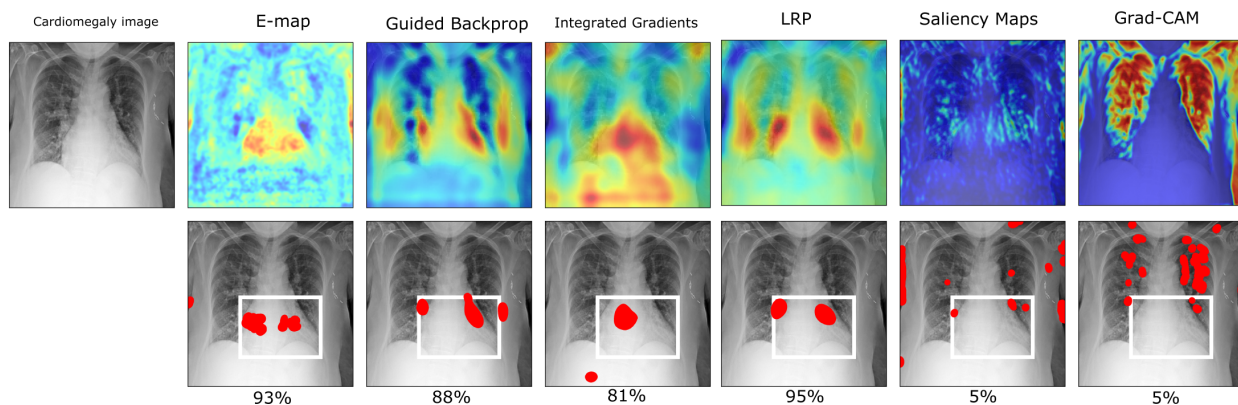


Figure 12: Example 1: Top row: E-map and heatmaps from different post-hoc interpretability methods. Bottom row: Percentage overlap with the top 1 percentile pixels (shown in red) and clinically annotated regions in the original abnormal image. The numbers signify the percentage overlap.

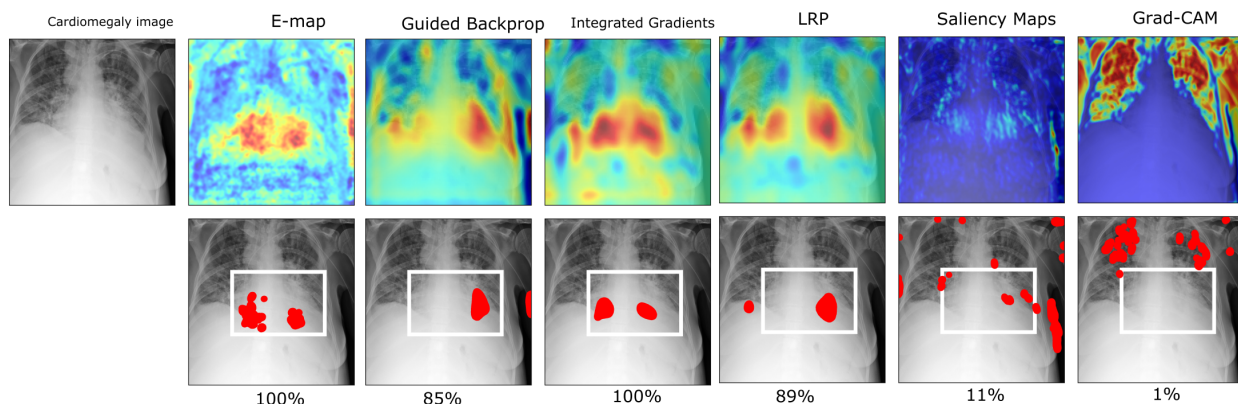


Figure 13: Example 2: Top row: E-map and heatmaps from different post-hoc interpretability methods. Bottom row: Percentage overlap with the top 1 percentile pixels (shown in red) and clinically annotated regions in the original abnormal image. The numbers signify the percentage overlap.

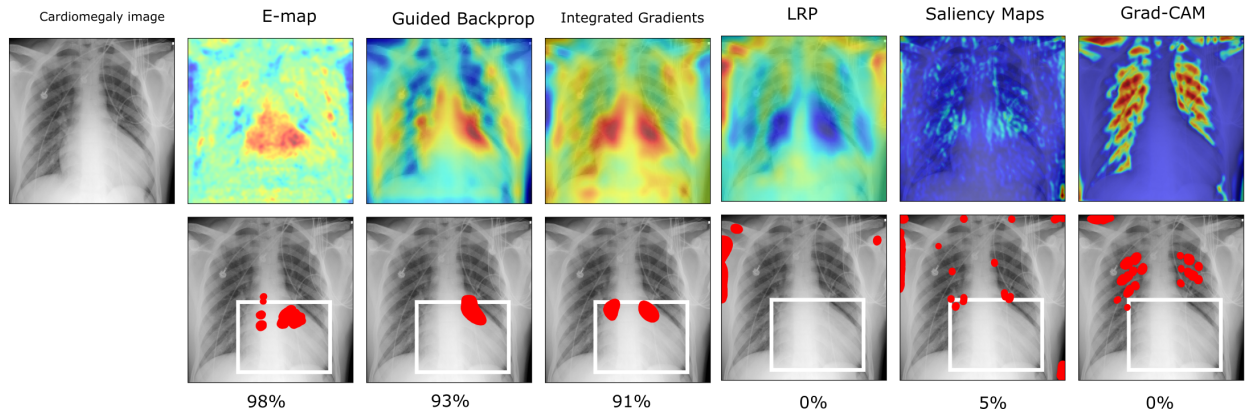


Figure 14: Example 3: Top row: E-map and heatmaps from different post-hoc interpretability methods. Bottom row: Percentage overlap with the top 1 percentile pixels (shown in red) and clinically annotated regions in the original abnormal image. The numbers signify the percentage overlap.

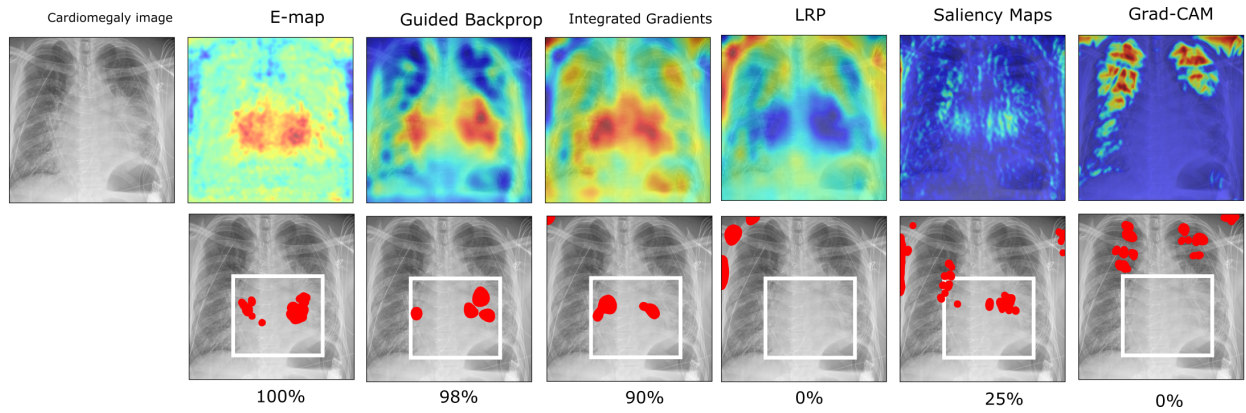


Figure 15: Example 4: Top row: E-map and heatmaps from different post-hoc interpretability methods. Bottom row: Percentage overlap with the top 1 percentile pixels (shown in red) and clinically annotated regions in the original abnormal image. The numbers signify the percentage overlap.

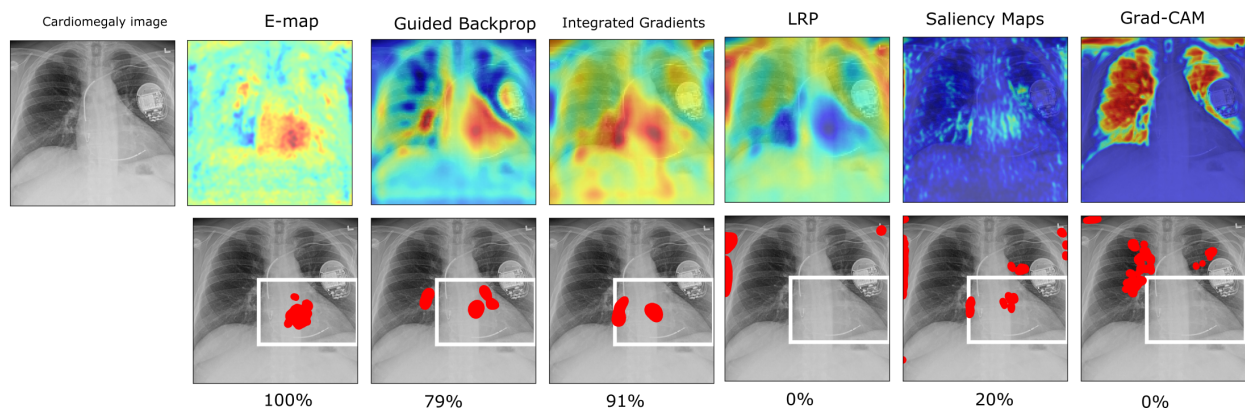


Figure 16: Example 5: Top row: E-map and heatmaps from different post-hoc interpretability methods. Bottom row: Percentage overlap with the top 1 percentile pixels (shown in red) and clinically annotated regions in the original abnormal image. The numbers signify the percentage overlap.